Magnetic and magnetotransport properties in the vanadium-based kagome metals DyV_6Sn_6 and HoV_6Sn_6

Xiang-Yu Zeng,[1,2] Huan Wang,[1,2] Xiao-Yan Wang,[1,2] Jun-Fa Lin,[1,2] Jing Gong,[1,2] Xiao-Ping Ma,[1,2] Kun Han,[1,2] Yi-Ting Wang,[1,2] Zheng-Yi Dai,[1,2] and Tian-Long Xia[1,2,3,4,*]

[1]*Department of Physics, Renmin University of China, Beijing 100872, China*
[2]*Beijing Key Laboratory of Opto-electronic Functional Materials & Micro-nano Devices, Renmin University of China, Beijing 100872, China*
[3]*Key Laboratory of Quantum State Construction and Manipulation (Ministry of Education), Renmin University of China, Beijing 100872, China*
[4]*Laboratory for Neutron Scattering, Renmin University of China, Beijing 100872, China*

(Received 27 July 2023; revised 10 January 2024; accepted 1 March 2024; published 13 March 2024)

Recently, the vanadium-based kagome metals RV_6Sn_6 (R=rare-earth) have attracted wide attention due to their novel magnetism and nontrivial topological properties. In this paper, the DyV_6Sn_6 and HoV_6Sn_6 single crystals were successfully synthesized and the magnetotransport measurements were performed to explore the physical properties. The magnetism along different directions in Dy/HoV_6Sn_6 were studied via magnetic susceptibility and magnetization measurements, which reveals ferromagnetic interaction along the c axis with magnetic transition temperature $T_m = 3.3$ K/2.7 K and antiferromagnetic interaction within the ab plane. Negative magnetoresistance was observed at small field and low temperature, which is attributed to the suppression of spin scattering. The nonlinear behavior of the Hall resistivity above T_m indicates that Dy/HoV_6Sn_6 are multiband systems while the S-shaped feature at low field and linear behavior at high filed below T_m imply the possible existence of anomalous Hall effect.

DOI: 10.1103/PhysRevB.109.104412

I. INTRODUCTION

The intermetallic compound with frustrated Kagome layers is an ideal platform to study the interplay of lattice geometry, magnetic orders, and electronic structures [1]. The topological nontrivial states with novel electronic properties have been studied in Kagome materials, such as the appearance of Dirac points, van Hove singularity, and geometry induced flat bands [2–5], frustrated magnetism [6–8], anomalous Hall responses [9–11], charge density waves (CDW) [12], etc. Recently, RMn_6X_6 (R = rare-earth; X = Sn, Ge) family materials with Mn-based Kagome lattice, crystallizing into a $HfFe_6Ge_6$-type structure ($P6/mmm$), have been investigated with their complex patterns of magnetism [13–23] and novel magnetotransport properties including anomalous Hall effect (AHE) [24–31] or topological Hall effect [27,28]. The rare-earth ions synergized with the magnetic Kagome lattice play an important role in the rich magnetic and topological properties. Recently, a similar series of vanadium-based Kagome metals RV_6Sn_6 (R = rare-earth) have attracted considerable attention as a new member of the Kagome materials [32–40]. The nonmagnetic V ions substitute Mn to form the Kagome layers, which may provide a more clear image to explore the interplay between the magnetism and electronic structures derived from the Kagome lattices via different rare-earth substitutions. ScV_6Sn_6 identifies a CDW [39–59] at 92 K, demonstrating that charge order is a common feature in partly filled d-orbital kagome systems. GdV_6Sn_6, HoV_6Sn_6, and TbV_6Sn_6 have been investigated by angle resolved photoemission spectroscopy measurements [34,38], from which Dirac point, saddle point, and flat band are observed, indicating the presence of nontrivial topological phases. Transport experiments on TbV_6Sn_6 [35,60] indicate that it holds a large anomalous Hall conductivity at 1.8 K to be approximately 2000 $\Omega^{-1} \cdot \mathrm{cm}^{-1}$, while it is difficult to perform detailed scaling analyses to identify the mechanism of the AHE due to the inadequate data of anomalous Hall resistivity at different temperatures below the Curie temperature (4.1 K). In YbV_6Sn_6, it shows typical heavy fermion properties above 2 K due to the Kondo effect on the Kramers doublet of Yb^{3+} ions in crystal electric field [40]. Thus, the pristine RV_6Sn_6 family materials are crucial to realize the interplay of magnetism and electronic structures, which deserves detailed transport studies.

Recently, the magnetic and electrical transport properties of $(Dy\text{-}Tm)V_6Sn_6$ have been reported [36,37]. The transition temperature of DyV_6Sn_6 and HoV_6Sn_6 is reported to be about 3.0 K and 2.5 K, while ErV_6Sn_6 and TmV_6Sn_6 do not show signs of magnetic order. However, detailed magnetoresistance and AHE studies on DyV_6Sn_6 and HoV_6Sn_6 need further investigation. In this paper, the physical properties via magnetic susceptibility, magnetization, and magnetotransport measurements were performed on the grown single crystals of DyV_6Sn_6 and HoV_6Sn_6. In Dy/HoV_6Sn_6, the transition metal V is nonmagnetic while the Dy/Ho ions form magnetic orders at $T_m = 3.3$ K/2.7 K. A canted or noncollinear

*tlxia@ruc.edu.cn

antiferromagnetic (AFM) structure is depicted below T_m, according to the anisotropic magnetic susceptibility and nonlinear behavior of magnetization results. Negative magnetoresistance (MR) is observed in Dy/HoV_6Sn_6 at low field and low temperature, which is attributed to the suppression of spin scattering. The nonlinear behavior of the Hall resistivity above T_m indicates that Dy/HoV_6Sn_6 are multiband systems. While below T_m, the S-shaped feature at low field and the linear Hall curves at high filed imply the possible existence of the anomalous Hall effect. The complex magnetic structures of Dy/HoV_6Sn_6 make them promising platforms to study exotic magnetotransport properties.

II. EXPERIMENTAL AND CRYSTAL STRUCTURE

The single crystals of DyV_6Sn_6 and HoV_6Sn_6 were grown from the Sn-flux method. The starting elements, dysprosium or holmium block, vanadium powder, and excess tin granules, were put into the corundum crucible and sealed in a quartz tube with a ratio of Dy/Ho:V:Sn = 1:6:20. The quartz tube was heated to 1125 °C at 60 °C/h and held for 20 h, then cooled to 780 °C at a rate of 1 °C/h, at which the excess Sn flux was separated from the crystals by centrifugation. The obtained crystals are a hexagonal platelike shape with length of about 1 ∼ 3 mm and thickness of 0.5 mm. Sn flux on the surfaces were removed by dilute hydrochloric acid. The atomic proportion of DyV_6Sn_6/HoV_6Sn_6 were checked to be Dy/Ho:V:Sn = 1:6:6 using energy dispersive x-ray spectroscopy (EDS, Oxford X-Max 50). The single crystal and powder x-ray diffraction (XRD) were collected from a Bruker D8 advance x-ray diffractometer using Cu K_α radiation. TOPAS-4.2 was employed for the refinement. The magnetic properties were measured with the vibrating sample magnetometer (VSM) option of the quantum design physical property measurement system (QD PPMS) using the polished crystal. The resistivity and Hall measurements were performed on a QD PPMS-14T using the standard six-probe method on a long flake crystal that is 0.1 mm thick.

III. RESULTS AND DISCUSSIONS

The crystal structure of RV_6Sn_6 is shown in Fig. 1(a), which crystallizes in a hexagonal $HfFe_6Ge_6$-type structure with *P*6/*mmm* (No. 191) space group. V-ion formed Kagome lattices are stacked along the *c* axis separated by two Sn layers and one RSn layer, whereas Sn ions occupy two different types of crystallographic sites, forming $[V_3Sn][RSn_2][V_3Sn]$ layers along the *c* axis. The powder XRD patterns of DyV_6Sn_6 and HoV_6Sn_6 are displayed in Figs. 1(b) and 1(c). As obtained from the XRD refinement of polycrystalline samples, DyV_6Sn_6 and HoV_6Sn_6 exhibit the $HfFe_6Ge_6$-type structure with the refined lattice parameters a = b = 5.519(1) Å, c = 9.184(3) Å and a = b = 5.516(9) Å, c = 9.186(4) Å, respectively. In addition, few impurity phases of V_3Sn and β-Sn are detected, as reported in previous studies [61]. It should be noted that few small peaks of V_3Sn indicate the traceable amount, contributing a negligible effect to the magnetic and magnetotransport properties. Figures 1(d) and 1(e) display the single crystal x-ray diffraction patterns of DyV_6Sn_6 and HoV_6Sn_6 with (001) reflections, and insets show the single crystals as a part of hexagonal samples. The temperature-dependent resistivity of DyV_6Sn_6 and HoV_6Sn_6 are displayed in Fig. 1(f), respectively, which exhibits a metallic behavior with residual resistivity ratio RRR = ρ(300 K)/ρ(2 K) ≈14/10. No signals of superconducting transition from V_3Sn and β-Sn are observed on the temperature-dependent resistivity. Thus, the transport properties of DyV_6Sn_6 and HoV_6Sn_6 reported here are believed to be intrinsic.

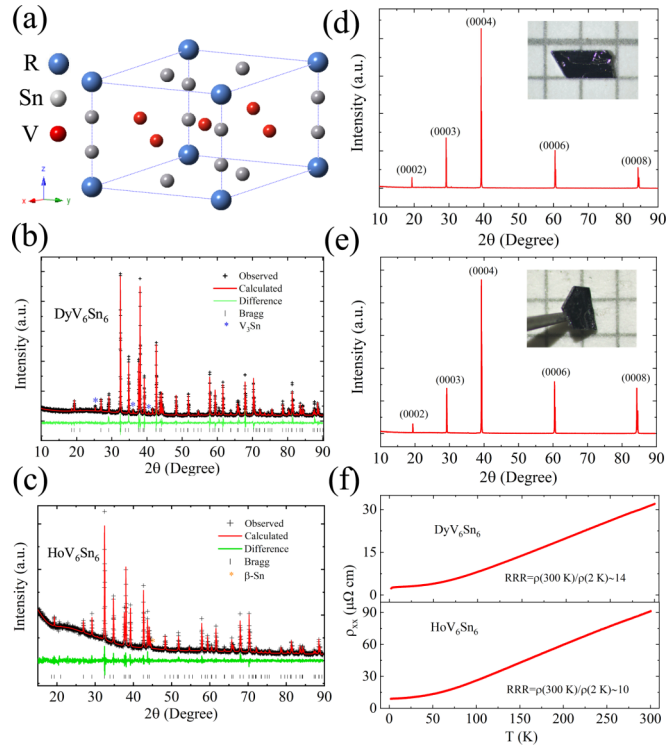

FIG. 1. (a) The crystal structure of RV_6Sn_6 (R = Dy,Ho) with the space group *P*6/*mmm* (No. 194). (b), (c) Powder XRD patterns with refinement. (d), (e) Single crystal XRD patterns of RV_6Sn_6 (R = Dy,Ho) with (00l) surface. Inset shows the typical single crystal. (f) Temperature-dependent resistivity ρ_{xx} of DyV_6Sn_6 and HoV_6Sn_6, respectively.

Figures 2(a)–2(d) display the temperature-dependent magnetization in DyV_6Sn_6 with a field of 50 Oe applied parallel and perpendicular to the *c* axis, respectively, indicating an anisotropic behavior of the magnetism. With H//c, the temperature-dependent magnetization of zero-field cooled (ZFC) and field-cooled (FC) curves both demonstrate the ferromagnetlike behaviors in which upturns appear at about 10 K and bifurcate at 3.3 K, as shown in Fig. 2(a). The behaviors indicate the emergence of ferromagnetic (FM) interactions at about 10 K and the formation of magnetic order at 3.3 K, respectively. With H ⊥ c, temperature-dependent ZFC and FC magnetization curves exhibit similar behaviors. It is noteworthy that the value of magnetization within the *ab* plane is almost four times larger than that along the *c* axis, indicating a slight anisotropy. In order to quantify the difference, a modified Curie-Weiss (CW) formula $\chi^{-1} = 1/(C/(T-T_\theta)+\chi(0))$ with an additional $\chi(0)$ term was employed to fit the inverse magnetic susceptibility χ^{-1} curves above 50 K as shown in Fig. 2(b). $\chi(0)$ originates from the

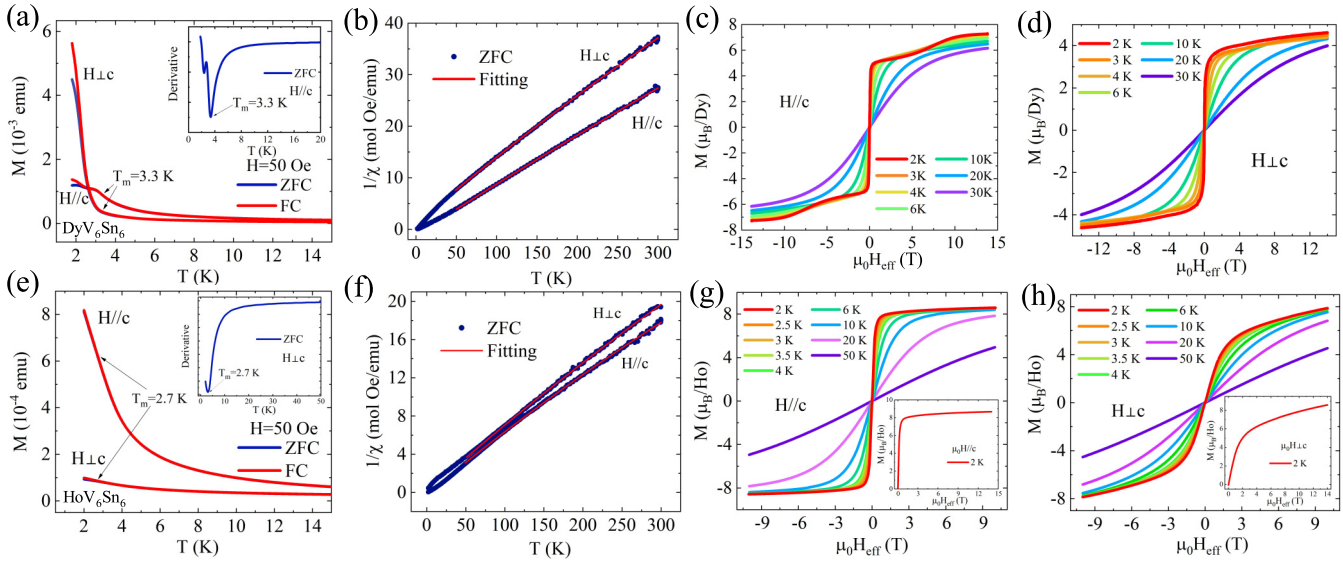

FIG. 2. (a), (e) Temperature-dependent magnetic susceptibilities of DyV_6Sn_6 and HoV_6Sn_6 with H//c and H ⊥ c under 50 Oe, respectively. (b), (f) The Curie-Weiss fittings of inverse susceptibility of DyV_6Sn_6 and HoV_6Sn_6 with H//c and H ⊥ c, respectively. (c), (g) Field-dependent magnetization of DyV_6Sn_6 and HoV_6Sn_6 along the *c* axis at various temperatures, respectively. (d), (h) Field-dependent magnetization of DyV_6Sn_6 and HoV_6Sn_6 along the *ab* plane at various temperatures, respectively.

Pauli and van Vleck paramagnetism, as well as diamagnetic signals of nucleus, and is independent of temperature. The obtained $\chi(0)$, T_θ, and Curie constant C are displayed in Table I. The values of the T_θ are 10.7 K and –8.2 K for H//c and H ⊥ c, suggesting the dominant FM interaction along the *c* axis and AFM interaction within the *ab* plane. The fitting generates the effective moment of $\mu^c_{\text{eff}} = 8.97\ \mu_B$/Dy and $\mu^{ab}_{\text{eff}} = 7.75\ \mu_B$/Dy, respectively, less than the spin-only moment of Dy^{3+} (10.6 μ_B). Furthermore, the field-dependent magnetization in both directions has been measured, as exhibited in Figs. 2(c) and 2(d), which further confirms the different magnetic interactions along different directions in DyV_6Sn_6. The magnetization along the *c* axis increases rapidly and seems to reach a first step of saturation at $\mu_0 H_{\text{eff}} = 0.6$ T. The steady slight rising remains until about 7.8 T before another significant increase appears and approaches the moment of 7.2 μ_B/Dy at 2 K and 14 T. This steplike magnetic transition behavior indicates that the magnetic structure may undergo transitions with increasing field [62,63]. Apparently, the moment on Dy^{3+} is not yet completely polarized under external field, compared with the effective moment obtained from the CW fitting. The nonmonotonic and unsaturated magnetization indicates the potential coexistence of AFM and FM interactions along the *c* axis. Within the *ab* plane, magnetization increases rapidly below 0.8 T and then increases monotonically up to 14 T where the moment reaches 4.6 μ_B/Dy, less than the effective moment extracted from Curie-Weiss fitting, signifying the system in a process of being uniformly polarized. Magnetic properties of HoV_6Sn_6 are also depicted via magnetization measurements in different directions, as shown in Figs. 2(e)–2(h). The temperature-dependent magnetization of ZFC (cyaneous line) and FC (red line) both exhibit an upturn below 2.7 K with H//c. In the other direction, M_{ab} is approximately six times weaker than M_c at low temperature, which indicates a slightly anisotropic behavior of the magnetism in HoV_6Sn_6. The fitting according to a modified Curie-Weiss formula yields $T^c_\theta = 3.2$ K with H//c and $T^{ab}_\theta = -0.6$ K with H ⊥ c, suggesting the dominance of FM interaction along the *c* axis and AFM interaction within the *ab* plane, as shown in Fig. 2(f). The corresponding parameters χ_0 and C are displayed in Table I. The magnetic field dependence of magnetization at various temperatures are plotted in Figs. 2(g) and 2(h) for H//c and H ⊥ c, respectively. The sharp increase of the magnetization at low field and saturated behavior at high field indicates the rapid polarization of the moments forming the FM component along the *c* axis. Within the *ab* plane, the slow and unsaturated rising of the magnetization demonstrates that AFM interaction is dominant. At 14 T, the maximum moment of 8.7 μ_B/Ho for H//c and 8.6 μ_B/Ho for H ⊥ c are obtained, which is lower than the effective moment extracted from Curie-Weiss fitting along respective directions, demonstrating that the field-polarized ferromagnetic state is still not reached at 14 T.

TABLE I. CurieWeiss fitting results of DyV_6Sn_6 and HoV_6Sn_6.

		$\chi(0)$	C	T_θ(K)	$\mu_{\text{eff}}(\mu_B)$
DyV_6Sn_6	H//c	0.0016	10.10	10.70	8.97
	H ⊥ c	0.0026	7.50	−8.19	7.75
HoV_6Sn_6	H//c	0.0072	14.54	3.27	10.77
	H ⊥ c	0.005	13.78	−0.68	10.50

As is shown, DyV_6Sn_6 and HoV_6Sn_6 both show magnetic anistropy at low temperatures, originating from the rare-earth anisotropy [64] which is usually described by the single-ion magnetic anisotropy theory [65]. The single-ion magnetic anisotropy is derived from the combination of SOC effect and crystal electric field (CEF) effect. The interaction between 4*f* ions and their interplay with surrounding atoms result in the different environments of crystal field, leading to different magnetic properties of RV_6Sn_6, as summarized

TABLE II. A summary of magnetic properties of $R\,V_6Sn_6$(R = Gd-Tm [33,36,37,60]): T_m is magnetic ordering temperatures; Weiss temperatures $T_\theta^{ab}(K)$ and $T_\theta^{c}(K)$; CEF parameter B_2^0 and easy magnetization direction. Asterisks indicate the values we obtained from the B_2^0 formula.

R	T_m(K)	T_θ^{ab} (K)	T_θ^{c} (K)	B_2^0(K)	Easy direction
Gd [37]	4.8	0.90	−2.50		
Gd [33]	5.2	7.56	7.76		
Tb [37]	4.3	−38.30	32.30	−1.40	*c* axis
Tb [60]	5.0	−40.40	33.10	−1.48*	*c* axis
Dy *this work*	3.3	−8.19	10.70	−0.25*	*c* axis
Dy [36]	3.0	−16.01	8.93	−0.33*	c axis
Dy [37]	2.9	−13.40	17.0	−0.40	*c* axis
Ho *this work*	2.7	−0.68	3.27	−0.05*	*c* axis
Ho [36]	2.5	−14.42	3.71	−0.21*	*c* axis
Ho [37]	2.3	−4.50	4.50	−0.10	*c* axis
Er [36]		4.42	−33.46	0.50*	*ab* plane
Er [37]		3.30	−29.90	0.40	*ab* plane
Tm [36]		12.69	−39.79	1.06*	*ab* plane
Tm [37]		10.30	−71.20	1.70	*ab* plane

in Table II, with our results from DyV_6Sn_6 and HoV_6Sn_6, which is similar to previous work [37]. According to the single-ion magnetic anisotropy theory, CEF effect is weak and $H_{CEF} = \sum_{l,m} B_l^m O_l^m$ determines the anisotropy of the 4*f* ions [65]. Here, B_l^m is the CEF parameter, which is determined by the symmetry of the crystal structure, and O_l^m is the equivalent operator, which is related to the angular momentum operators. If only the term with l = 2, m = 0 is considered, the sign of the CEF parameter B_2^0 determines whether the direction of magnetization is along the *c* axis. According to the point charge model, the CEF parameters are determined by the Weiss temperature in the *ab* plane and the *c* direction, and the total angular momentum J of the material $B_2^0 = \frac{10(T_\theta^{ab}-T_\theta^{c})}{3(2J-1)(2J+3)}$ [66,67]. Based on the Curie-Weiss fitting results in our work and previous studies, the values of B_2^0 are calculated, as shown in Table II. For DyV_6Sn_6 and HoV_6Sn_6, as B_2^0 <0, the angular momentum is parallel to the *c* axis, and the *c* axis is the easy axis, which is consistent with our experimental results, as shown in Figs. 2(c), 2(d), 2(g), and 2(h).

According to the above reported magnetic properties, the coexistence of FM and AFM interactions make the DyV_6Sn_6 and HoV_6Sn_6 complex and intriguing materials. Here, we performed the MR ($MR = (\rho(B) - \rho(0))/\rho(0)$) and Hall measurements at various temperatures to investigate their electrical properties. Figures 3(a) and 3(e) show the MR for DyV_6Sn_6 and HoV_6Sn_6, respectively. In DyV_6Sn_6, at low temperatures (T < 10 K), MR decreases rapidly with field increasing until a critical field ($B_c = \pm 0.65$ T at 2 K as an example) is reached, then it turns to increase and presents decurved behavior at high field.

The negative MR and the departure from quadratic behavior suggest that magnetism plays an essential role in the transport properties. Above 20 K, far away from the magnetic transition temperature 3.3 K, DyV_6Sn_6 exhibits the positive and quadratic MR as usually expected. As the two main components of MR, positive MR is dominated by the orbital effects deriving from the cyclotron motion of the electrons caused by Lorentz force, while negative MR may stem from multiple factors, such as the suppression of magnetic scattering, chiral anomaly, or current jetting, etc. Indeed, chiral anomaly is observable only when B//I and current jetting can be avoided via improving the experimental techniques (We used a highly symmetrical electrode and evenly coated silver adhesive for measurements). The comparison between MR and field-dependent magnetization is displayed in Fig. 3(b), in which B_c is coincident with the first saturated field of magnetization (labeled with black dotted lines). Dy^{3+} moments are polarized at B_c, forming an ordered state, which reduces the magnetic scattering of conduction electrons, resulting in the negative MR. As the field increases, the orbital MR dominates and competes with the magnetism induced negative MR, leading to a reclinate behavior at high field. In HoV_6Sn_6, the MR exhibits similar behavior as those in DyV_6Sn_6:

$$\Delta\sigma_{xy} = \left(\frac{n_h\mu_h^2}{1+(\mu_h B)^2} - \frac{n_e\mu_e^2}{1+(\mu_e B)^2}\right)eB. \quad (1)$$

In order to demonstrate the electrical properties and characteristics of carriers in DyV_6Sn_6 and HoV_6Sn_6, Hall resistivity ρ_{yx} has been measured with the field parallel to the *c* axis. In Figs. 3(c) and 3(g), Hall resistivities present the nonlinear behavior, indicating the multiband characteristics. Significantly, at 2 K, ρ_{yx} exhibits a cambered form at low field and becomes completely linear above 6 T, which is in accord with the behavior of AHE in magnetic materials. In order to verify the possible AHE in Dy/HoV_6Sn_6, the component of normal Hall $\rho_{xy}^N = R_0B$ is extracted by the linear fitting of the high-field region (6–14 T) according to $\rho_{yx} = R_0B + \rho_{yx}^A$. R_0 is the normal Hall coefficient and $\rho_{yx}^A = 0.247$ μΩ cm (DyV_6Sn_6) and 0.325 μΩ cm (HoV_6Sn_6) are the anomalous hall components. The fitting curves are displayed in the insets of Figs. 3(d) and 3(h). The AHE singal (red dotted line) is extracted via subtracting the normal Hall from the total Hall resistivity, which is resemblant to magnetization curves. AHE is closely related to the topological nontrivial band structures which has large Berry curvature. In DyV_6Sn_6 and HoV_6Sn_6, Dirac points and surface states, which contribute a large Berry curvature resulting in the anomalous Hall effect, are observed

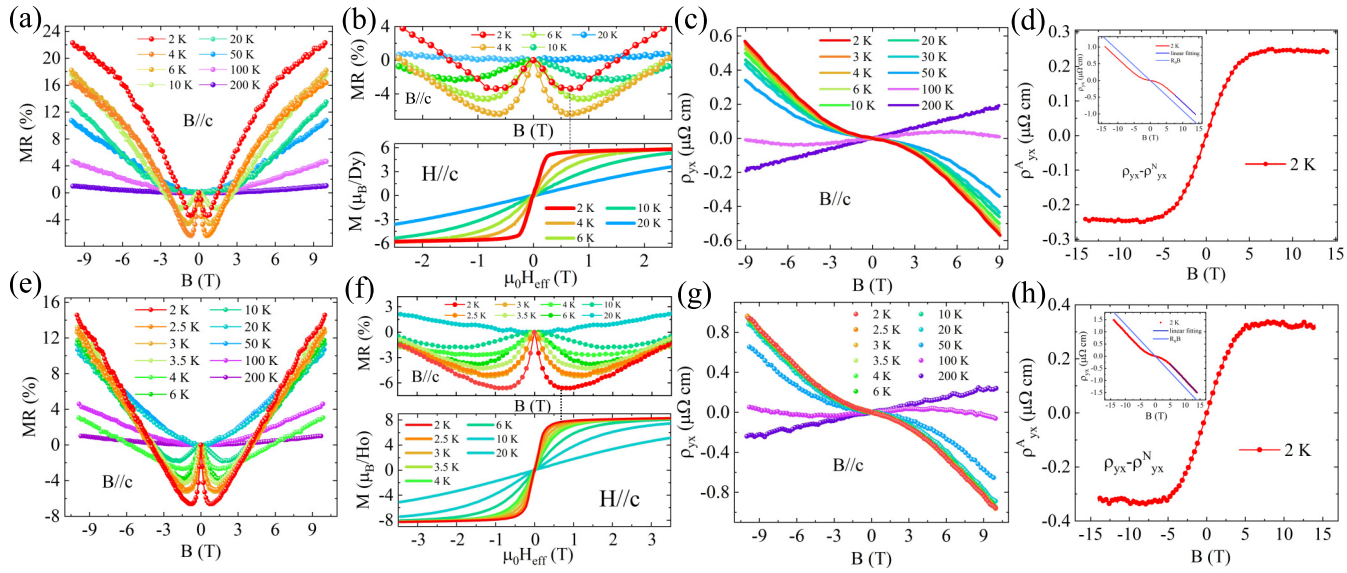

FIG. 3. (a), (e) Magnetic field-dependent MR at different temperatures of DyV_6Sn_6 and HoV_6Sn_6, respectively. (b), (f) Upper: Enlarged view around zero field of Fig. (a) and Fig. (e). Lower: Corresponding field-dependent magnetization curves of DyV_6Sn_6 and HoV_6Sn_6, respectively. (c), (g) Magnetic field-dependent Hall resistivity at various temperatures of DyV_6Sn_6 and HoV_6Sn_6, respectively. (d), (h) The field-dependent anomalous Hall resistivity of DyV_6Sn_6 and HoV_6Sn_6, respectively. Inset shows the linear fitting at the high field and normal Hall resistivity $\rho_{yx}^{N} = R_0B$.

in previous ARPES measurements [34,38]. In magnetic materials, the relation $\rho_{yx}^{A} \propto \rho_{xx}^{\alpha}$ is usually employed to estimate the mechanism of AHE. However, the anomalous Hall resistivity ρ_{yx}^{A} and resistivity ρ_{xx} below T_m can only provide insufficient data, making it impossible to take more detailed scaling analyses according to the conventional methods to identify the mechanisms of AHE.

Above T_m, the Hall resistivity reveals a nonlinear behavior at various temperatures and the linear behavior at high field gradually disappears. The change of the normal Hall effect indicates that DyV_6Sn_6 and HoV_6Sn_6 may transform from a single-band to a multiband system, possibly due to the vanishment of the magnetic order that changes the band structure above T_m. It is normal that the magnetic orders exert great influence on the band structures so that the fermi surface and the characteristics of carriers are changed accordingly [68]. Therefore, it is suitable to fit the Hall conductivity with the two-band model. Figures 4(a) and 5(a) display the field-dependent Hall conductivity. The fitting curves from Eq. (1) match well with the experimental results, from which the concentrations and mobilities are extracted, reflecting the temperature-dependent change of the electronic structures [Figs. 4(b) and 4(c), and Figs. 5(b) and 5(c)]. The $n_{e,h}$ and $\mu_{e,h}$ represent the concentration and mobility of electrons or holes, respectively. As the temperature decreases, the electron concentration of DyV_6Sn_6 first increase and then fluctuate below 10 K, while hole concentration has an opposite changing tendency. High mobility of the two types of carriers both increase with lowering temperature and show a similar change below 10 K. The striking consistency of the temperature-dependent concentration and mobility suggests

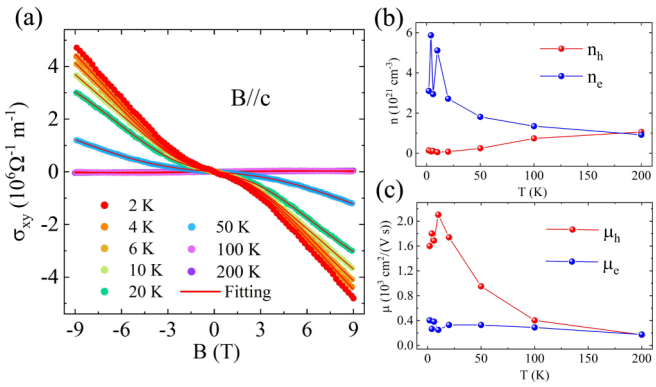

FIG. 4. (a) Field dependence of the Hall conductivity ($\sigma_{xy} = \rho_{yx}/((\rho_{yx})^2 + (\rho_{xx})^2)$) of DyV_6Sn_6 at various temperatures. (b), (c) The temperature dependence of carrier concentration and mobility.

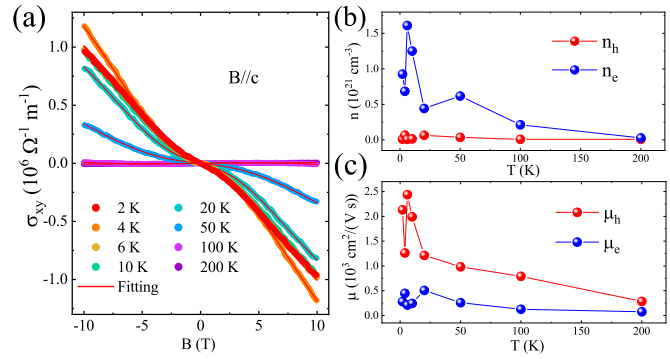

FIG. 5. (a) Field dependence of the Hall conductivity ($\sigma_{xy} = \rho_{yx}/((\rho_{yx})^2 + (\rho_{xx})^2)$) of HoV_6Sn_6 at various temperatures. (b), (c) The temperature dependence of carrier concentration and mobility.

that magnetic properties have crucial influence on electronic structures. In addition, $\sigma_{xy} = \rho_{yx}/\rho_{xx}^2 + \rho_{yx}^2$ contains field-dependent resitivity components. Obviously, the behavior of MR is strongly affected by the magnetism in DyV_6Sn_6, which is also reflected at the fitting of the Hall conductivity and extracted $n_{e,h}$ and $\mu_{e,h}$. As discussed above, the fluctuant behavior of temperature-dependent $n_{e,h}$ and $\mu_{e,h}$ below 10 K indicates that the appearance of magnetic interaction significantly modulates the electronic structures, which further affect the characteristics of carriers. At 2 K, $n_e = 3.1 \times 10^{21}$ cm^{-3}, $n_h = 1.4 \times 10^{20}$ cm^{-3}, $\mu_e = 405$ cm^2/Vs and $\mu_h = 1600$ cm^2/Vs for DyV_6Sn_6. $n_e = 9.3 \times 10^{20}$ cm^{-3}, $n_h = 8.9 \times 10^{18}$ cm^{-3}, $\mu_e = 280$ cm^2/Vs, and $\mu_h = 2132$ cm^2/Vs for HoV_6Sn_6. The multiband fitting reveals the large electron pockets with lower carrier mobility, and a high mobility hole pocket with much smaller carrier density. Generally, the conductivity of electrons and holes could be simply written as $\sigma_e = n_e\mu_e e$ and $\sigma_h = n_h\mu_h e$, respectively. The imbalance between σ_e and σ_h confirms the electron-dominant transport in DyV_6Sn_6 and HoV_6Sn_6.

IV. SUMMARY

In summary, single crystals of DyV_6Sn_6 and HoV_6Sn_6 are synthesized which crystallize in hexagonal structures with V-Kagome layers. The magnetism along different directions are studied via magnetization and magnetotransport measurements. Dy/HoV_6Sn_6 show FM interaction along the c axis with magnetic transition temperature $T_m = 3.3$ K/2.7 K and AFM interaction within the ab plane. The noncollinear field-dependent magnetization along the c axis indicates that DyV_6Sn_6 has complex magnetic structure with the coexistence of FM and AFM interactions. Magnetoresistance measurements further confirm the dominant ferromagnetism along the c axis. Hall resistivity reveals that Dy/HoV_6Sn_6 are multiband systems with high mobility and possess the feature of anomalous Hall effect below T_m. Furthermore, previous work confirmed that HoV_6Sn_6 is topological magnetic semimetals with Dirac points and nontrivial topological surface states. DyV_6Sn_6 and HoV_6Sn_6 are analogous platforms which require further studies of explicit spin configuration and band structure to study the relation between topology and magnetism in Kagome materials.

ACKNOWLEDGMENTS

This work is supported by the National Key R&D Program of China (Grant No. 2019YFA0308602), the National Natural Science Foundation of China (Grants No. 12074425 and No. 11874422), the Fundamental Research Funds for the Central Universities, and the Research Funds of Renmin University of China (No. 23XNKJ22).

[1] K. Ohgushi, S. Murakami, and N. Nagaosa, Spin anisotropy and quantum Hall effect in the kagomé lattice: Chiral spin state based on a ferromagnet, Phys. Rev. B **62**, R6065 (2000).

[2] I. Mazin, H. O. Jeschke, F. Lechermann, H. Lee, M. Fink, R. Thomale, and R. Valentí, Theoretical prediction of a strongly correlated Dirac metal, Nat. Commun. **5**, 4261 (2014).

[3] L. Ye, M. Kang, J. Liu, F. Von Cube, C. R. Wicker, T. Suzuki, C. Jozwiak, A. Bostwick, E. Rotenberg, D. C. Bell *et al.*, Massive Dirac fermions in a ferromagnetic kagome metal, Nature (London) **555**, 638 (2018).

[4] Z. Liu, F. Liu, and Y.-S. Wu, Exotic electronic states in the world of flat bands: From theory to material, Chin. Phys. B **23**, 077308 (2014).

[5] M. Kang, L. Ye, S. Fang, J.-S. You, A. Levitan, M. Han, J. I. Facio, C. Jozwiak, A. Bostwick, E. Rotenberg *et al.*, Dirac fermions and flat bands in the ideal kagome metal FeSn, Nat. Mater. **19**, 163 (2020).

[6] J.-X. Yin, S. S. Zhang, G. Chang, Q. Wang, S. S. Tsirkin, Z. Guguchia, B. Lian, H. Zhou, K. Jiang, I. Belopolski *et al.*, Negative flat band magnetism in a spin-orbit-coupled correlated kagome magnet, Nat. Phys. **15**, 443 (2019).

[7] N. J. Ghimire, R. L. Dally, L. Poudel, D. Jones, D. Michel, N. T. Magar, M. Bleuel, M. A. McGuire, J. Jiang, J. Mitchell *et al.*, Competing magnetic phases and fluctuation-driven scalar spin chirality in the kagome metal YMn_6Sn_6, Sci. Adv. **6**, eabe2680 (2020).

[8] M. Kang, S. Fang, L. Ye, H. C. Po, J. Denlinger, C. Jozwiak, A. Bostwick, E. Rotenberg, E. Kaxiras, J. G. Checkelsky *et al.*, Topological flat bands in frustrated kagome lattice CoSn, Nat. Commun. **11**, 4004 (2020).

[9] T. Kida, L. A. Fenner, A. A. Dee, I. Terasaki, M. Hagiwara, and A. S. Wills, The giant anomalous Hall effect in the ferromagnet Fe_3Sn_2 a frustrated kagome metal, J. Phys.: Condens. Matter **23**, 112205 (2011).

[10] E. Liu, Y. Sun, N. Kumar, L. Muechler, A. Sun, L. Jiao, S.-Y. Yang, D. Liu, A. Liang, Q. Xu *et al.*, Giant anomalous Hall effect in a ferromagnetic kagome-lattice semimetal, Nat. Phys. **14**, 1125 (2018).

[11] Q. Wang, Y. Xu, R. Lou, Z. Liu, M. Li, Y. Huang, D. Shen, H. Weng, S. Wang, and H. Lei, Large intrinsic anomalous Hall effect in half-metallic ferromagnet $Co_3Sn_2S_2$ with magnetic Weyl fermions, Nat. Commun. **9**, 3681 (2018).

[12] K. Chen, N. Wang, Q. Yin, Y. Gu, K. Jiang, Z. Tu, C. Gong, Y. Uwatoko, J. Sun, H. Lei *et al.*, Double superconducting dome and triple enhancement of T_c in the kagome superconductor CsV_3Sb_5 under high pressure, Phys. Rev. Lett. **126**, 247001 (2021).

[13] G. Venturini, B. C. El Idrissi, and B. Malaman, Magnetic properties of RMn_6Ge_6 (R = Sc, Y, Gd- Tm, Lu) compounds with $HfFe_6Ge_6$ type structure, J. Magn. Magn. Mater. **94**, 35 (1991).

[14] Y. Amako, T. Yamamoto, M. Misawa, H. Yoshie, and H. Nagai, Magnetic properties of YMn_6Ge_6, J. Magn. Magn. Mater. **140-144**, 1029 (1995).

[15] B. Malaman, G. Venturini, B. C. El Idrissi, and E. Ressouche, Magnetic properties of $NdMn_6Sn_6$ and $SmMn_6Sn_6$ compounds from susceptibility measurements and neutron diffraction study, J. Alloys Compd. **252**, 41 (1997).

[16] D. Gorbunov, M. Kuzmin, K. Uhlivrova, M. Žáček, M. Richter, Y. Skourski, and A. Andreev, Magnetic properties of a $GdMn_6Sn_6$ single crystal, J. Alloys Compd. **519**, 47 (2012).

[17] Z. Chen, M. Li, C. Liu, Z. Ma, Y. Han, J. Gao, W. Wei, Z. Sheng, and H. Du, Magnetic Domain Structure in Ferromagnetic Kagome Metal $DyMn_6Sn_6$, Front. Phys. **9**, 685510 (2021).

[18] M. Koyama, Y. Narumi, S. Yoshii, K. Kindo, L. Zhang, E. Bruck, K. Buschow, F. De Boer, C. Lefevre, and G. Venturini, Magnetic study on single crystals of YMn_6Ge_6 and $LuMn_6Ge_6$, J. Alloys Compd. **408-412**, 161 (2006).

[19] M. Kelemen, P. Rosch, E. Dormann, and K. Buschow, Spiral spin structures of RMn_6Ge_6(R=Gd, Tb, Dy), J. Magn. Magn. Mater. **223**, 253 (2001).

[20] K. Uhlířová, F. de Boer, V. Sechovsky, S. Yoshii, Y. Nakagawa, M. Hagiwara, K. Kindo, and G. Venturini, Magnetism of $DyMn_6Ge_6$, J. Magn. Magn. Mater. **316**, e422 (2007).

[21] K. Uhlirova, V. Sechovsky, F. R. De Boer, S. Yoshii, K. Nishikawa, M. Hagiwara, K. Kindo, and G. Venturini, Magnetism of $ErMn_6Ge_6$, J. Phys. Conf. Ser. **51**, 123 (2006).

[22] A. Mar, C. Lefevre, and G. Venturini, Anisotropic transport properties measured in $HoMn_6Ge_6$ single crystals, J. Magn. Magn. Mater. **269**, 380 (2004).

[23] S. Yoshii, K. Kindo, L. Zhang, E. Bruck, K. Buschow, F. De Boer, C. Lefevre, and G. Venturini, Magnetization study on single-crystalline $TbMn_6Ge_6$, J. Alloys Compd. **408-412**, 173 (2006).

[24] K. Uhlířová, V. Sechovsky, F. R. de Boer, S. Yoshii, T. Yamamoto, M. Hagiwara, C. Lefevre, and G. Venturini, Magnetic properties and Hall effect of single-crystalline YMn_6Sn_6, J. Magn. Magn. Mater. **310**, 1747 (2007).

[25] T. Asaba, S. M. Thomas, M. Curtis, J. D. Thompson, E. D. Bauer, and F. Ronning, Anomalous Hall effect in the kagome ferrimagnet $GdMn_6Sn_6$, Phys. Rev. B **101**, 174415 (2020).

[26] W. Ma, X. Xu, J.-X. Yin, H. Yang, H. Zhou, Z.-J. Cheng, Y. Huang, Z. Qu, F. Wang, M. Z. Hasan *et al.*, Rare Earth Engineering in RMn_6Sn_6 (R = Gd-Tm, Lu) Topological Kagome Magnets, Phys. Rev. Lett. **126**, 246602 (2021).

[27] G. Dhakal, F. C. Kabeer, A. K. Pathak, F. Kabir, N. Poudel, R. Filippone, J. Casey, A. P. Sakhya, S. Regmi, C. Sims *et al.*, Anisotropically large anomalous and topological Hall effect in a kagome magnet, Phys. Rev. B **104**, L161115 (2021).

[28] Q. Wang, K. J. Neubauer, C. Duan, Q. Yin, S. Fujitsu, H. Hosono, F. Ye, R. Zhang, S. Chi, K. Krycka *et al.*, Field-induced topological Hall effect and double-fan spin structure with a c-axis component in the metallic kagome antiferromagnetic compound YMn_6Sn_6, Phys. Rev. B **103**, 014416 (2021).

[29] L. Gao, S. Shen, Q. Wang, W. Shi, Y. Zhao, C. Li, W. Cao, C. Pei, J.-Y. Ge, G. Li *et al.*, Anomalous Hall effect in ferrimagnetic metal RMn_6Sn_6 (R = Tb, Dy, Ho) with clean Mn kagome lattice, Appl. Phys. Lett. **119**, 092405 (2021).

[30] F. Kabir, R. Filippone, G. Dhakal, Y. Lee, N. Poudel, J. Casey, A. P. Sakhya, S. Regmi, R. Smith, P. Manfrinetti *et al.*, Unusual magnetic and transport properties in $HoMn_6Sn_6$ kagome magnet, Phys. Rev. Mater. **6**, 064404 (2022).

[31] H. Zhou, M. Shi, Y. Huang, W. Ma, X. Xu, J. Wang, and S. Jia, Metamagnetic transition and anomalous Hall effect in Mn-based kagome magnets RMn_6Ge_6 (R = Tb-Lu), Phys. Rev. Mater. **7**, 024404 (2023).

[32] H. Ishikawa, T. Yajima, M. Kawamura, H. Mitamura, and K. Kindo, GdV_6Sn_6: A multi-carrier metal with non-magnetic 3d-electron Kagome bands and 4 f-electron magnetism, J. Phys. Soc. Jpn. **90**, 124704 (2021).

[33] G. Pokharel, S. M. Teicher, B. R. Ortiz, P. M. Sarte, G. Wu, S. Peng, J. He, R. Seshadri, and S. D. Wilson, Electronic properties of the topological kagome metals YV_6Sn_6 and GdV_6Sn_6, Phys. Rev. B **104**, 235139 (2021).

[34] S. Peng, Y. Han, G. Pokharel, J. Shen, Z. Li, M. Hashimoto, D. Lu, B. R. Ortiz, Y. Luo, H. Li *et al.*, Realizing kagome band structure in two-dimensional kagome surface states of RV_6Sn_6 (R = Gd, Ho), Phys. Rev. Lett. **127**, 266401 (2021).

[35] E. Rosenberg, J. M. DeStefano, Y. Guo, J. S. Oh, M. Hashimoto, D. Lu, R. J. Birgeneau, Y. Lee, L. Ke, M. Yi *et al.*, Uniaxial ferromagnetism in the kagome metal TbV_6Sn_6, Phys. Rev. B **106**, 115139 (2022).

[36] X. Zhang, Z. Liu, Q. Cui, Q. Guo, N. Wang, L. Shi, H. Zhang, W. Wang, X. Dong, J. Sun *et al.*, Electronic and magnetic properties of intermetallic kagome magnets RV_6Sn_6 (R = Tb-Tm), Phys. Rev. Mater. **6**, 105001 (2022).

[37] J. Lee and E. Mun, Anisotropic magnetic property of single crystals RV_6Sn_6(R = Y, Gd-Tm, Lu), Phys. Rev. Mater. **6**, 083401 (2022).

[38] Y. Hu, X. Wu, Y. Yang, S. Gao, N. C. Plumb, A. P. Schnyder, W. Xie, J. Ma, and M. Shi, Tunable topological Dirac surface states and van Hove singularities in kagome metal GdV_6Sn_6, Sci. Adv. **8**, eadd2024 (2022).

[39] H. W. S. Arachchige, W. R. Meier, M. Marshall, T. Matsuoka, R. Xue, M. A. McGuire, R. P. Hermann, H. Cao, and D. Mandrus, Charge density wave in kagome lattice intermetallic ScV_6Sn_6, Phys. Rev. Lett. **129**, 216402 (2022).

[40] K. Guo, J. Ye, S. Guan, and S. Jia, Triangular Kondo lattice in YbV_6Sn_6 and its quantum critical behavior in a magnetic field, Phys. Rev. B **107**, 205151 (2023).

[41] X. Zhang, J. Hou, W. Xia, Z. Xu, P. Yang, A. Wang, Z. Liu, J. Shen, H. Zhang, X. Dong *et al.*, Destabilization of the charge density wave and the absence of superconductivity in ScV_6Sn_6 under high pressures up to 11 GPa, Materials **15**, 7372 (2022).

[42] D. W. Kim, S. Liu, C. Wang, H. W. Nam, G. Pokharel, S. D. Wilson, J.-H. Cho, and S. J. Moon, Infrared probe of the charge density wave gap in ScV_6Sn_6, Phys. Rev. B **108**, 205118 (2023).

[43] S. Mozaffari, W. R. Meier, R. P. Madhogaria, N. Peshcherenko, S.-H. Kang, J. W. Villanova, H. W. S. Arachchige, G. Zheng, Y. Zhu, K.-W. Chen *et al.*, Universal sublinear resistivity in vanadium kagome materials hosting charge density waves, arXiv:2305.02393.

[44] S. Blanco-Canosa, A. Korshunov, H. Hu, D. Subires, Y. Jiang, D. Calugaru, X. Feng, A. Rajapitamahuni, C. Yi, S. Roychowdhury *et al.*, Softening of a flat phonon mode in the kagome ScV_6Sn_6, Nat. Commun. **14**, 6646 (2023).

[45] J. M. DeStefano, E. Rosenberg, O. Peek, Y. Lee, Z. Liu, Q. Jiang, L. Ke, and J.-H. Chu, Pseudogap behavior in charge density wave kagome material ScV_6Sn_6 revealed by magneto-transport measurements, npj Quantum Mater. **8**, 65 (2023).

[46] Y. Hu, J. Ma, Y. Li, D. J. Gawryluk, T. Hu, J. Teyssier, V. Multian, Z. Yin, Y. Jiang, S. Xu *et al.*, Phonon promoted charge density wave in topological kagome metal ScV_6Sn_6, arXiv:2304.06431.

[47] Y. Gu, E. T. Ritz, W. R. Meier, A. Blockmon, K. Smith, R. P. Madhogaria, S. Mozaffari, D. Mandrus, T. Birol, and J. L. Musfeldt, Phonon mixing in the charge density wave state of ScV_6Sn_6, npj Quantum Mater. **8**, 58 (2023).

[48] T. Hu, H. Pi, S. Xu, L. Yue, Q. Wu, Q. Liu, S. Zhang, R. Li, X. Zhou, J. Yuan *et al.*, Optical spectroscopy and band

structure calculations of the structural phase transition in the vanadium-based kagome metal ScV_6Sn_6, Phys. Rev. B **107**, 165119 (2023).

[49] S. Cheng, Z. Ren, H. Li, J. Oh, H. Tan, G. Pokharel, J. M. DeStefano, E. Rosenberg, Y. Guo, Y. Zhang *et al.*, Nanoscale visualization and spectral fingerprints of the charge order in ScV_6Sn_6 distinct from other kagome metals, npj Quantum Mater. **9**, 14 (2024).

[50] H. Hu, Y. Jiang, D. Călugăru, X. Feng, D. Subires, M. G. Vergniory, C. Felser, S. Blanco-Canosa, and B. A. Bernevig, Kagome materials I: Sg 191, ScV_6Sn_6. Flat phonon soft modes and unconventional CDW formation: Microscopic and effective theory, arXiv:2305.15469.

[51] Z. Guguchia, D. Gawryluk, S. Shin, Z. Hao, C. Mielke III, D. Das, I. Plokhikh, L. Liborio, K. Shenton, Y. Hu *et al.*, Hidden magnetism uncovered in charge ordered bilayer kagome material ScV_6Sn_6, arXiv:2304.06436.

[52] M. Tuniz, A. Consiglio, D. Puntel, C. Bigi, S. Enzner, G. Pokharel, P. Orgiani, W. Bronsch, F. Parmigiani, V. Polewczyk *et al.*, Dynamics and resilience of the charge density wave in a bilayer kagome metal, arXiv:2302.10699.

[53] S. Liu, C. Wang, S. Yao, Y. Jia, Z. Zhang, and J.-H. Cho, Driving mechanism and dynamic fluctuations of charge density waves in the kagome metal ScV_6Sn_6, arXiv:2308.13796.

[54] S. Cao, C. Xu, H. Fukui, T. Manjo, Y. Dong, M. Shi, Y. Liu, and C. Cao, and Y. Song, Competing charge-density wave instabilities in the kagome metal ScV_6Sn_6, Nat. Commun. **14**, 7671 (2023).

[55] C. Yi, X. Feng, N. Mao, P. Yanda, S. Roychowdhury, Y. Zhang, C. Felser, and C. Shekhar, Quantum oscillations revealing topological band in kagome metal ScV_6Sn_6, Phys. Rev. B **109**, 035124 (2024).

[56] S.-H. Kang, H. Li, W. R. Meier, J. W. Villanova, S. Hus, H. Jeon, H. W. S. Arachchige, Q. Lu, Z. Gai, J. Denlinger *et al.*, Emergence of a new band and the Lifshitz transition in kagome metal ScV_6Sn_6 with charge density wave, arXiv:2302.14041.

[57] H. Tan and B. Yan, Abundant lattice instability in kagome metal ScV_6Sn_6, Phys. Rev. Lett. **130**, 266402 (2023).

[58] G. Pokharel, B. R. Ortiz, L. Kautzsch, S. J. Gomez Alvarado, K. Mallayya, G. Wu, E.-A. Kim, J. P. C. Ruff, S. Sarker, and S. D. Wilson, Frustrated charge order and cooperative distortions in ScV_6Sn_6, Phys. Rev. Mater. **7**, 104201 (2023).

[59] W. R. Meier, R. P. Madhogaria, S. Mozaffari, M. Marshall, D. E. Graf, M. A. McGuire, H. W. S. Arachchige, C. L. Allen, J. Driver, H. Cao *et al.*, Tiny Sc allows the chains to rattle: Impact of Lu and Y doping on the charge-density wave in ScV_6Sn_6, J. Am. Chem. Soc. **145**, 20943 (2023).

[60] G. Pokharel, B. Ortiz, J. Chamorro, P. Sarte, L. Kautzsch, G. Wu, J. Ruff, and S. D. Wilson, Highly anisotropic magnetism in the vanadium-based kagome metal TbV_6Sn_6, Phys. Rev. Mater. **6**, 104202 (2022).

[61] L. Romaka, Y. Stadnyk, V. Romaka, P. Demchenko, M. Stadnyshyn, and M. Konyk, Peculiarities of component interaction in {Gd, Er}-V-Sn ternary systems at 870 K and crystal structure of RV_6Sn_6 stannides, J. Alloys Compd. **509**, 8862 (2011).

[62] S. Jiang, Y. Luo, Z. Ren, Z. Zhu, C. Wang, X. Xu, Q. Tao, G. Cao, and Z. Xu, Metamagnetic transition in $EuFe_2As_2$ single crystals, New J. Phys. **11**, 025007 (2009).

[63] C. Detlefs, F. Bourdarot, P. Burlet, P. Dervenagas, S. L. Bud'ko, and P. C. Canfield, Ordering wave vectors of metamagnetic states in $HoNi_2B_2C$: One dimension is not enough, Phys. Rev. B **61**, R14916 (2000).

[64] R. Skomski and D. Sellmyer, Anisotropy of rare-earth magnets, J. Rare Earths **27**, 675 (2009).

[65] E. Bauer and M. Rotter, Magnetism of complex metallic alloys: Crystalline electric field effects, in *Properties and Applications of Complex Intermetallics* (World Scientific, Singapore, 2010), pp. 183–248.

[66] Y.-L. Wang, Crystal-field effects of paramagnetic Curie temperature, Phys. Lett. A **35**, 383 (1971).

[67] P. Boutron, Exact calculation of the paramagnetic susceptibility of a single crystal with arbitrary crystal field and exchange interactions, Phys. Rev. B **7**, 3226 (1973).

[68] P. E. Siegfried, H. Bhandari, D. C. Jones, M. P. Ghimire, R. L. Dally, L. Poudel, M. Bleuel, J. W. Lynn, I. I. Mazin, and N. J. Ghimire, Magnetization-driven lifshitz transition and charge-spin coupling in the kagome metal YMn_6Sn_6, Commun. Phys. **5**, 58 (2022).